




## Double-slit experiment with multiple vortex beams

Mairikena Aili, Pan Liu, Xiao-Xiao Chen , Qing-Yuan Wu, Zhe Meng, Jia-Zhi Yang ,  
Jian Li, and An-Ning Zhang \*

*Center for Quantum Technology Research and Key Laboratory of Advanced Optoelectronic Quantum Architecture and Measurements,  
School of Physics, Beijing Institute of Technology, Haidian District, Beijing 100081, People's Republic of China*

 (Received 23 November 2022; revised 26 February 2023; accepted 4 January 2024; published 29 January 2024)

The orbital angular momentum (OAM) of a vortex beam has already found significant potential applications in both quantum and classical communication systems. In this study, a realization of a double-slit experiment using a Sagnac interferometer is conducted for the detection and discrimination of vortex beams. Based on the advantages of convenient and adjustable double-slit parameters of our device, we detected multiple vortex beams carrying different OAM modes and superpositions of OAM modes under laser and single-photon illumination. We also analyzed the influence of the slit parameters on the interference pattern of the vortex beams. The results show that by comparing the differences in these interference patterns, we can achieve the measurement of topological charge and complete distinction of OAM states carried by the vortex beams. Our study contributes to coding research on laser and quantum communication.

DOI: [10.1103/PhysRevA.109.013521](https://doi.org/10.1103/PhysRevA.109.013521)

### I. INTRODUCTION

Orbital angular momentum (OAM) [1], as an important degree of freedom (DOF), has garnered increasing attention and significant development in various domains. The OAM-carrying beams, commonly referred to as vortex beams, have an azimuthal phase of  $e^{im\phi}$ , where  $m$  denotes the topological charge (TC) and  $\phi$  denotes the azimuthal angle, which carries a quantized OAM of  $m\hbar$  per photon. Clearly, the range of  $m$  is  $-\infty$ – $+\infty$ , indicating that quantum information can be stored in high-dimensional OAM states of single photons. They provide powerful capabilities for applications in quantum communication [2,3] and computing [4]. Furthermore, vortex beams open avenues for potential applications in various fields, including optical manipulation and trapping [5,6], high precision optical metrology [7,8], nonlinear optics [9], chiral microstructures [10], high-dimensional entanglement [11,12], quantum information processing [13,14], remote sensing [15], and quantum imaging [16].

It is well known that measurement of the OAM states of vortex beams holds considerable significance in applications utilizing OAM-carrying vortex beams [17,18]. Considered one of the most seminal experiments in wave optics, Young's double-slit interference [19] provided the first explanation of the wave property of light. It has been successfully performed in various systems and different DOFs of light, such as space [20], time [21], and polarization [22,23]. With the deepening and diversification of studies, an increasing number of variables have been added to the study of Young's double-slit interference, such as OAM [24]. Recently, several studies have been devoted to Young's double-slit experiment using vortex beams for a better understanding and interpretation

of the nature of vortex beams in interference phenomena. For instance, Sztul and Alfano proposed Young's double-slit interference with vortex beams for the first time and highlighted that the twisted interference fringes were closely related to the TC of vortex beams [24]. Furthermore, Li and Qi *et al.* detected radially and azimuthally polarized vector vortex beams [25,26] using Young's double-slit interference. Chen *et al.* conducted Young's double-slit experiment using partially coherent vortex beams [27]. Studies have already highlighted that the interference fringes of vortex beams are closely related to slit parameters [24]. However, no detailed experimental demonstration on the effects of slit parameters was presented, because it is difficult to modulate the slit parameters with the conventional structure of double-slit interference. In this article, a realization of the double-slit experiment is described. Compared with our previous work for detecting single-photon OAM states based on the Sagnac interferometer (in Ref. [28]), the present work has the following advantages or differences. (i) The interferometric methods of both works are different. The double slit is realized by positioning a single slit at the midpoint of a Sagnac interferometer. A single slit is inserted into the interferometer to mimic Young's double-slit experiment. Interference experiments in the double-slit and the Sagnac interferometer domain are entirely different and have different properties to demonstrate OAM potential. (ii) The capabilities of experimental setup. The previous work has capabilities for manipulating the single-photon OAM states and sorting the photon. And the present work has the capability for distinguishing the multiple OAM states simultaneously and can easily control the parameters related to double slits. (iii) OAM modes that these two setups can distinguish are different. The previous work can only recognize mixed-mode OAM states, while the current work can also recognize conjugate mode and single-mode OAM states. (iv) The imaging methods of both works at the

\*Corresponding author: [anningzhang@bit.edu.cn](mailto:anningzhang@bit.edu.cn)

single-photon level are different. For the previous one we used the raster scanning imaging (RSI) to detect OAM states. But, in the present work, we have used the single-pixel imaging (SPI).

Here we investigate numerically and experimentally the distribution of interference fringes of multiple OAM states with a laser and single-photon source in a double-slit setup. Moreover, we show the interference fringes of OAM states with various slit parameters. The results demonstrate that our scheme is capable of distinguishing not only the individual OAM states but also the TC carried by the vortex beams. This study provides another insight into the double-slit interference of vortex beams and paves the way for measuring OAM states with different modes-based applications ranging from classical to quantum physics.

## II. THEORY

As a good approximation, the vortex beam can be expressed in the Laguerre–Gaussian (LG) mode. An LG beam propagating along the  $z$  axis (with radial mode index  $p = 0$  and azimuthal index  $m$ ) can be expressed as follows [29,30]:

$$E_{0,m}(r, \phi) = \frac{L_{0,m}}{\sqrt{w(z)}} \left( \frac{r\sqrt{2}}{w(z)} \right)^{|m|} \exp\left[-\frac{r^2}{w^2(z)}\right] \exp(-im\phi) \times \exp\left[-ik_0 \frac{r^2 z}{2(z^2 + z_R^2)}\right] \times \left[ -i(|m| + 1) \tan^{-1}\left(\frac{z}{z_R}\right) \right], \quad (1)$$

where  $(r, \phi)$  denote the polar coordinates in the transverse plane;  $L_{0,m}$  denotes the normalization constant.  $w(z) = w_0 \sqrt{1 + (z/z_R)^2}$  denotes the beam waist.

In a previous study [24,27], OAM states' interference with the same polarization in a double slit was investigated. The OAM states are formulated as follows:

$$|\Psi^\pm\rangle_P = |\pm m\rangle|P\rangle, \quad (2)$$

where  $|\pm m\rangle$  denotes the TC of the spatial field and  $|P\rangle$  denotes any polarized state. In fact, the interference results would occur for any arbitrary input polarization.

In this study, we replaced the states with single OAM modes, which are formulated as follows:

$$|\Psi^\pm\rangle = |\pm m\rangle|D\rangle. \quad (3)$$

$|D\rangle$  denotes the  $+45^\circ$ -polarized state instead of any polarized state. The state  $|\Psi^\pm\rangle$  in our Sagnac-type interferometer is equivalent to the states  $|\Psi^\pm\rangle_P$  in Young's double-slit interferometer [as shown in Fig. 1(a)].

Due to the spiral wavefront of the LG beam, when an LG beam with a single OAM modes passes through a Sagnac-type double-slit interferometer, there is a phase difference between the double slits. Figure 1(b) shows the geometry construction of the double slit in the  $x, y$  plane with slit width  $b$  and slit separation  $2a$ . Figure 1(c) shows the phase distribution of the single-mode LG beams along the  $y$  axis on double slits when  $m = 1$ . In accordance with [24], we call the phase along the left side of the slit  $\phi_1(y)$  and the phase along the right slit

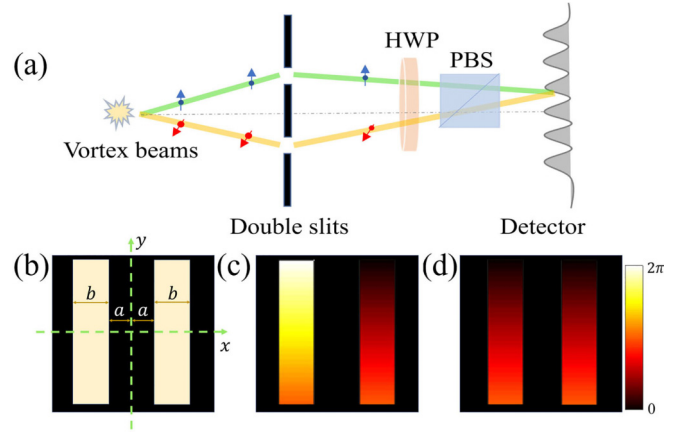


FIG. 1. (a) Conventional Young's double-slit experiment of vortex beam.  $H$  and  $V$  polarization of the vortex beam pass through the up and down slits of a double slit and are analyzed by the detector after a half wave plate (HWP) and polarizing beam splitter (PBS). (b) Geometry construction of double slit. (c) Phase distribution of the single-mode OAM states  $|\Psi^+\rangle$  in the double slit. (d) Phase distribution of the conjugate mode OAM states  $|\Phi\rangle$  in the double slit.

$\phi_2(y)$ . The phase difference between the double-diffraction slits at the same  $y$  can be deduced as follows:

$$\delta\phi(y) = \phi_2(y) - \phi_1(y) = -m\pi - 2m \arctan \frac{y}{a}. \quad (4)$$

The phase difference of double slits changes from 0 (bottom) to  $-2m\pi$  (top) with  $-m\pi$  at the center on the double slit as shown in Fig. 1(c). According to the optical path difference theory, the intensity distribution of LG beams after the double slit is determined as follows:

$$I(x, y) \propto \cos^2\left(\frac{2\pi ax}{d\lambda} + \frac{\delta\phi(y)}{2}\right), \quad (5)$$

where  $\lambda$  denotes the wavelength of the incident light and  $d$  denotes the distance between the slit and observation screen. It also can be determined that the fringe spacing is  $\Delta x = \lambda d/2a$ . Thus the fringes are equidistant and parallel to the central fringe. The variation in the interference pattern in the  $x$  direction is determined as follows:

$$x = \frac{\lambda dm}{2a\pi} \arctan \frac{y}{a}. \quad (6)$$

From this equation, we observe that when  $y/a$  tends from  $-\infty$  to  $+\infty$ ,  $x$  changes from  $x_- = -\lambda dm/4a$  to  $x_+ = \lambda dm/4a$ . This implies that the fringe is twisted. The twist amount is equal to  $\lambda dm/2a$ , which is proportional to the absolute value of  $m$ . The twist direction depends on the sign of  $m$ . These features are useful for measuring the TC of beams.

The conventional structure of double-slit interference is polarization independent and interference can occur for any input polarization. However, our device is polarization dependent and can distinguish the polarization  $|H\rangle$  and  $|V\rangle$  of the beam. The OAM and polarization of photons are combined in an inseparable manner, which makes it possible to distinguish the OAM modes and detect more types of vortex beams. Therefore, we investigate the conjugate mode OAM state  $|\Phi\rangle$

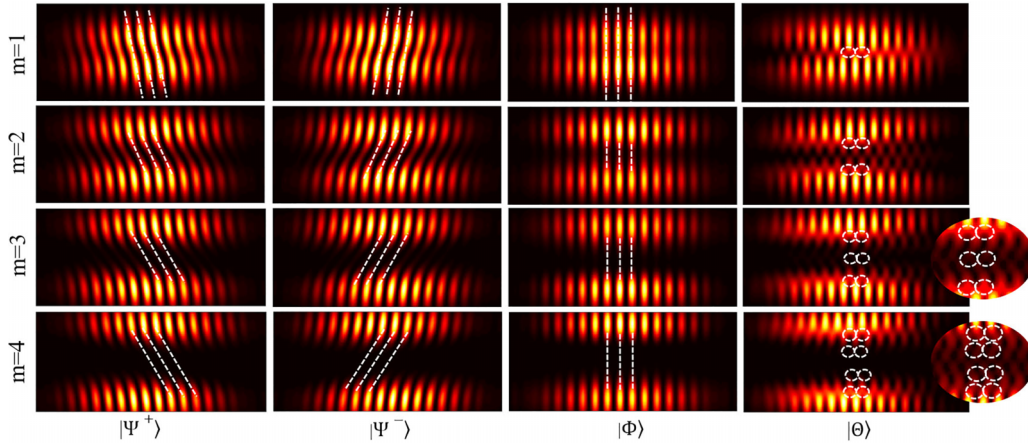


FIG. 2. Theoretical simulation results for double-slit interference fringes of vortex beams with OAM states  $|\Psi^+\rangle$ ,  $|\Psi^-\rangle$ ,  $|\Phi\rangle$ , and  $|\Theta\rangle$ . Each row corresponds to the OAM states with charge  $m = 1$ ,  $m = 2$ ,  $m = 3$ ,  $m = 4$  on the basis  $H + V$ .

[31] (that is the superposition of two modes that are conjugate to each other) and mixed-mode OAM state  $|\Theta\rangle$  [32], which are formulated as follows:

$$|\Phi\rangle = \frac{1}{\sqrt{2}}(|m\rangle|H\rangle + i|-m\rangle|V\rangle), \quad (7)$$

$$|\Theta\rangle = \frac{1}{2}(|m\rangle + |-m\rangle)|H\rangle - \frac{i}{2}(|m\rangle - |-m\rangle)|V\rangle. \quad (8)$$

Figure 2 shows the simulation result of the above states of vortex beams passing through a double-slit based on Fresnel diffraction theory [33]. Here, we take slit separation  $a = 450 \mu\text{m}$ , slit width  $b = 50 \mu\text{m}$ , wavelength is  $810 \text{ nm}$ , and the distance between slits and screen is  $78 \text{ cm}$ . For the vortex beam with single-mode OAM states shown in the first and second columns of Fig. 2, the interferograms appear as twisted fringes. For  $|\Psi^+\rangle$ , the interference fringes are twisted to the right and, for  $|\Psi^-\rangle$ , the interference fringes are twisted to the left. This indicates that the twist direction depended on the sign of  $m$ . As the value of  $m$  increases, the twisting of the fringes becomes increasingly evident as shown by the dotted white line. Thus  $m$  can be evaluated from the twisting amount of the interference fringes. These features are the same as those in Refs. [24,27], indicating that our scheme can also work as a Young's double slit. The features of the remaining two states are unique to our setup because of the ability of the device to distinguish the polarization of the beam.

The third column of Fig. 2 shows the interference fringes of the vortex beams with conjugate mode OAM state  $|\Phi\rangle$  passing through a double slit. In this case, the opposite-sign ( $\pm m$ ) OAM modes passed through the double slit. It can be observed that the interference pattern is a straight stripe with equal spacing. This is related to the phase distribution of the vortex beams in the slit. There is no phase difference in the helical phases carried by photons at the same height ( $y$ ) in the left and right slits, as shown in Fig. 1(d). As the  $m$  increases, the interference fringes are separated into up and down regions. The separation degree is proportional to  $m$ . Thus, through the size of the black area in the middle of the fringe, we can qualitatively distinguish each OAM state.

The fourth column of Fig. 2 shows the interference fringes of the vortex beams with mixed-mode OAM state  $|\Theta\rangle$  passing through a double slit. In this case, the superposed OAM modes pass through the double slit. When  $m = 1$ , the interference fringes appear to be dislocated in the upper and lower stripes and have one node in the  $y$  direction, as indicated by the dotted white circle in the pattern. For the case  $m = 2$ , the interference fringes appear as two dislocations in the upper and lower regions and have two nodes in the  $y$  direction. When  $m = 3$ , an additional misplacement and an additional node appear in the middle region of the interference fringes compared to the case  $m = 2$ . As  $m$  increases, more dislocations appear in the interferogram. The node number is equal to  $m$ . Thus these features enabled the identification of the  $m$  values of vortex beams and can qualitatively distinguish each OAM state.

### III. EXPERIMENT

The experimental setup for investigating the double-slit interference of vortex beams based on the Sagnac-type double-slit interferometer is shown in Fig. 3. In the classical laser experiment, we use an  $808 \text{ nm}$  fiber laser with  $2 \text{ mW}$  output power and a charge-coupled device (CCD, ZY-PHC2K), at an exposure time of  $100 \mu\text{s}$ . In the quantum imaging experiment, as shown in Fig. 3(a), a collimated  $405 \text{ nm}$  continuous wave diode laser with  $20 \text{ mW}$  output power is used. It pumps a periodically poled potassium titanyl phosphate crystal to produce heralded single photons at  $810 \text{ nm}$  based on type-II spontaneous parametric down-conversion. To validate the performance of the single-photon source, we measured the value of the second-order correlation function  $g^{(2)}$  to be  $0.0103$ . In the step of single-photon OAM state preparation, as shown in Fig. 3(b), we prepare the initial state encoded with both polarization and OAM using quarter wave plates (QWPs), vortex retarder (VR) [28,34] (one charge with  $m = 2$  and two charges with  $m = 1$ ), and HWPs. More HWPs and VRs are used for the generation of the higher-order OAM states of the vortex beam. In Fig. 3(e), we take the preparation of the single-mode OAM state  $|\Psi^+\rangle$  as an example, with specific preparation

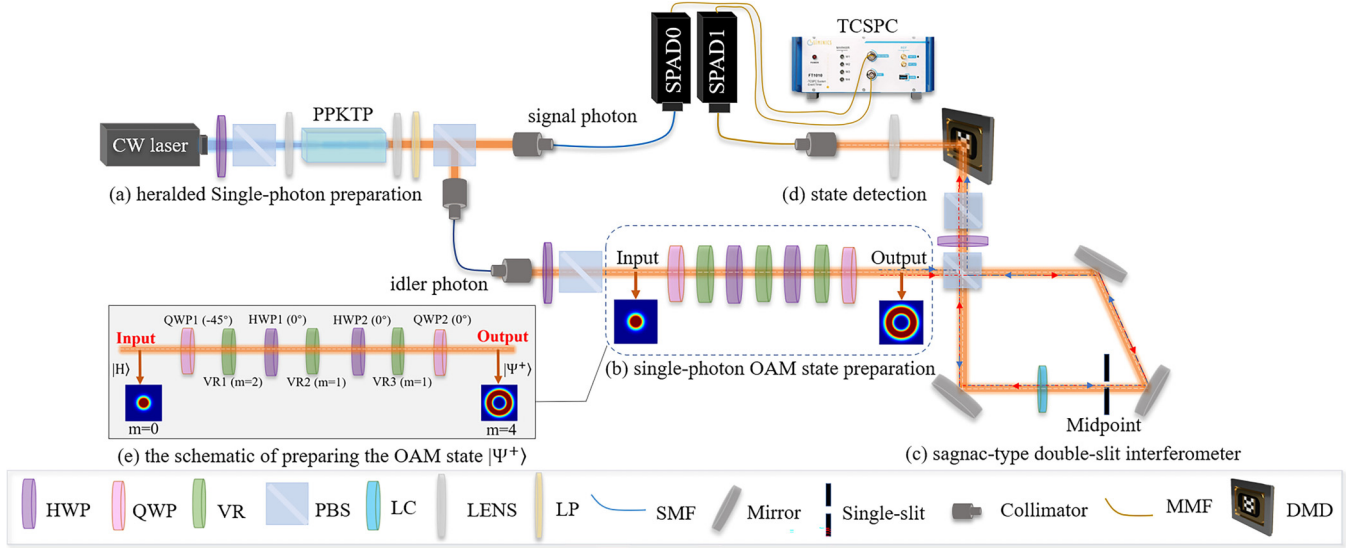


FIG. 3. Experimental setup for the detection and discrimination of single-photon vortex beams. See the text for details. The abbreviation of the equipment is as follows: PPKTP, periodically poled potassium titanyl phosphate; SMF, single-mode fiber; MMF, multimode fiber; HWP, half wave plates; QWP, quarter wave plates; VR, vortex retarder; LC, liquid crystal; note that the marking lines (the red and blue dashed) we have depicted in (c) are simply to show that the different parts of the clockwise and counterclockwise beams pass through the slit. In the inside of the interferometer, the beams propagating clockwise and counterclockwise are totally overlapped.

details as follows. (The input is H-polarized Gaussian light, whose photons' state is  $|m=0\rangle|H\rangle \xrightarrow{\text{QWP1}(-45^\circ)} |m=0\rangle|R\rangle \xrightarrow{\text{VR1}(m=2)} |m=2\rangle|L\rangle \xrightarrow{\text{HWP1}(0^\circ)} |m=2\rangle|R\rangle \xrightarrow{\text{VR2}(m=1)} |m=3\rangle|L\rangle \xrightarrow{\text{HWP2}(0^\circ)} |m=3\rangle|R\rangle \xrightarrow{\text{VR3}(m=1)} |m=4\rangle|L\rangle \xrightarrow{\text{QWP2}(0^\circ)} |m=4\rangle|H\rangle + |m=4\rangle|V\rangle$ . Here, the function of  $m$ -order VR is described as  $|R, m'\rangle \xrightarrow{m\text{-order VR}} |L, m'+m\rangle$ ,  $|L, m'\rangle \xrightarrow{m\text{-order VR}} |R, m'-m\rangle$ , where,  $|R\rangle \propto |H\rangle + i|V\rangle$  and  $|L\rangle \propto |H\rangle - i|V\rangle$  represent the right- and left-circularly polarized states, respectively. The methods of preparing a single-photon source and the multiple OAM states are the same as described in Ref. [28].

In the third step, as shown in Fig. 3(c), the beam enters the Sagnac-type double-slit interferometer comprising three mirrors (M) and a PBS. A single PBS serves as the input and output gates of the interferometer. The horizontal ( $|H\rangle$ ) and vertical ( $|V\rangle$ ) polarized beam (bonds with the DOF of OAM) split from the PBS propagate inside the interferometer along the same optical line but in the clockwise (as indicated by the red dashed line) and counterclockwise (as indicated by the blue dashed line) directions. A liquid crystal (LC) placed in the path of the Sagnac interferometer is used to impart a fixed phase difference of  $e^{i\theta}$  between  $|H\rangle$  and  $|V\rangle$ . A single slit is placed in the midpoint of the Sagnac interferometer and slightly offset from the optical axis to the inside of the interferometer. For a beam propagating clockwise, the slit is located on the right side of the optical axis (indicated by the white dashed line) along the propagation direction of the beam. For the counterclockwise path of the beam, the slit is located on the left side of the optical axis along the beam direction. It is evident that the two beams in the red and blue dashed lines pass through the single slit. However, they are symmetrical about the optical axis outside the interferometer. This

single slit selects different OAM modes of the vortex beam cross section propagating in clockwise and counterclockwise directions. Thus our Sagnac interferometer can be regarded as a wavefront-splitting interferometer, which is equivalent to Young's double-slit interference device, as shown in Fig. 1(a). After being reflected by the mirrors, the two beams meet again and pass out of the other port of the PBS. Thereafter, HWP and PBS are used to realize the projection measurement of  $H+V$ . Interference fringes appear because we cannot distinguish the path information of beams on a measurement basis. Note that the double-slit separation is twice the offset of the slit from the optical axis and there will be no Young's fringes if the slit is placed on the optical axis.

In the last step of our experiment, we detected the vortex beams using single-pixel imaging (SPI) [35–37] based on compressed sensing. It is capable of imaging under low-light conditions [38–40] and uses dynamic illumination to obtain the spatial information. Photons of the OAM states are emitted from the last PBS and directly received by the SPI device for imaging, as shown in Fig. 3(d). The SPI device comprises a digital mirror device (DMD, TI-DLP7000), lens, single-photon avalanche photodiode (SPAD, Excelitas Technologies SPCM-800-14-FC), and time-correlated single-photon counting (TCSPC, SIMINICS FT1040). The DMD has an array of  $1024 \times 768$  micromirrors. The side length of each square mirror is  $13.68 \mu\text{m}$  and those mirrors can be controlled to tilt. Photons emanating from the last PBS are reflected by the Hadamard pattern displayed on the DMD at a frame rate of 0.1 Hz and collected by the SPAD after passing through a lens. The role of TCSPC is to convert light intensity signals into digital signals with time resolution (64 ps accuracy). In our single-photon experiment, the interference results are obtained using  $64 \times 64$  pixels for the quick-sort Hadamard SPI scheme, which quickly sorts Hadamard patterns of any

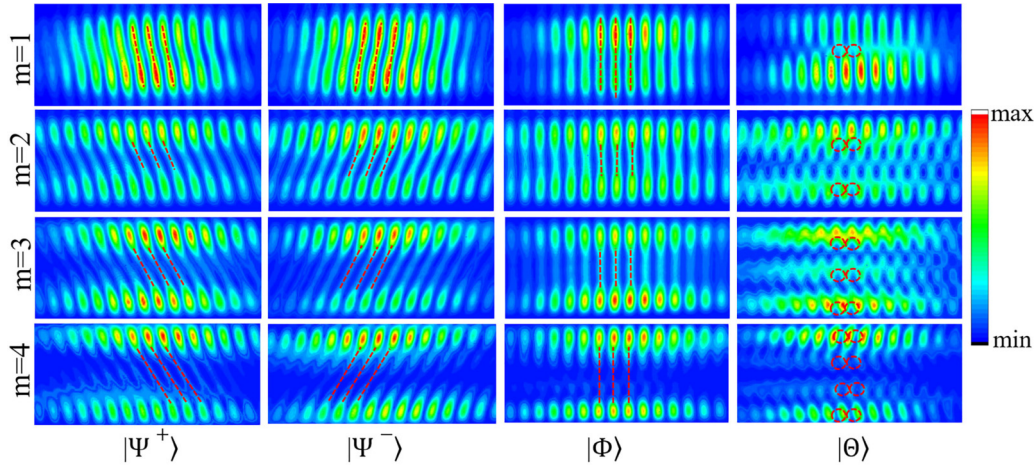


FIG. 4. Experimental results for laser double-slit interference fringes of vortex beams with OAM states  $|\Psi^+\rangle$ ,  $|\Psi^-\rangle$ ,  $|\Phi\rangle$ , and  $|\Theta\rangle$  under slit separation  $a = 450 \mu\text{m}$  and slit width  $b = 50 \mu\text{m}$ , when  $m = 1$ ,  $m = 2$ ,  $m = 3$ , and  $m = 4$ .

size. The images reconstructed by total variation augmented Lagrangian alternating direction algorithm (TVAL3) at the sampling ratio of 50%. The sampling time for each pattern on the DMD is 10 s. The number of samples is 2048 times. The count rate at the detector is approximately 200 000 photons per s. The dark count is 100 cps.

#### IV. RESULTS AND DISCUSSION

Figure 4 shows the experimental results of the laser double-slit interference pattern for multiple vortex beams under various TC values of  $m = 1, 2, 3$ , and 4. Each column corresponds to the different mode OAM states  $|\Psi^+\rangle$ ,  $|\Psi^-\rangle$ ,  $|\Phi\rangle$ , and  $|\Theta\rangle$  for a fixed value of slit separation  $a = 450 \mu\text{m}$  and slit width  $b = 50 \mu\text{m}$ . It can be observed that the interference pattern is unique to each OAM state. The single-mode OAM states  $|\Psi^+\rangle$  and  $|\Psi^-\rangle$ , shown in the first and second columns in Fig. 4, have opposite twisting directions owing to the sign of the  $m$ . The larger the value of  $|m|$ , the clearer the distortion as shown by the dotted black line. Thus the OAM states with different valued  $m$  can be distinguish from the twisting amount of the interference fringes. For the conjugate mode OAM states  $|\Phi\rangle$  as shown in the third column of Fig. 4, the interference fringes are a straight stripe with equal spacing. As  $m$  increased, the separation interval in the middle of the interference fringes are increased. For the mixed-mode OAM state  $|\Theta\rangle$  as shown in the fourth column of Fig. 4, interference fringes appear as dislocations. When  $m = 1$ , the fringes appear to be misplaced in the upper and lower stripes and have one node along the  $y$  direction. In the case of  $m = 2$ , two dislocations appear in the upper and lower regions and have two nodes along the  $y$  direction. With an increase in  $m$ , more dislocations appeared in the interferogram as shown in the numerical results. Based on this relationship, we can qualitatively determine the TC from the interference intensity. These features are the same with simulated results. Therefore, this double-slit experiment can serve as an alternative method for distinguishing the OAM states of vortex beams.

In fact, the double-slit pattern of vortex beams has some correlation with the slit parameters [24] because the slit

parameters affect the changes in the phase across the slits. In a conventional Young's double-slit structure, manipulation of the interference effects of vortex beams based on slit parameters is not convenient and it is difficult to maintain the same slit width. Our Sagnac-type double-slit device is suitable to accurately control slit parameters  $a$  and  $b$  and affects the interference pattern of OAM states. Below, we present and analyze the experimental results in detail.

Figure 5 shows the interference patterns of the different mode OAM states  $|\Psi^+\rangle$ ,  $|\Phi\rangle$ , and  $|\Theta\rangle$  with  $m = 2$  passing through the double slit under various slit widths  $b = 50 \mu\text{m}$ ,  $150 \mu\text{m}$ ,  $250 \mu\text{m}$ , and  $350 \mu\text{m}$  for slit separations of  $a = 400 \mu\text{m}$  and  $a = 600 \mu\text{m}$ . The state  $|\Psi^-\rangle$  is omitted because it has the same properties as  $|\Psi^+\rangle$ . It is difficult to maintain the same slit width in a conventional Young's double-slit experiment and the width of the double slits is usually not the same. Only one slit is used in our experiment. In other words, our double slits are the same. Slit width  $b$  is easily controlled by a commercial single-slit device. The results clearly show that the interferograms of the three types of vortex beams changed as the slit width changed. As the slit width increased, the number of visible fringes decreased and the width of the interference fringe changed. Therefore, the small valued slit width will be more effective for distinguishing the OAM states. For the slit separation  $a$ , the interference properties of the OAM states are well represented when the slit separation is  $a = 400 \mu\text{m}$ . Thus slit parameters are essential to improve the quality for distinguishing the OAM states.

Figure 6 shows the interference intensities of the different mode OAM states  $|\Psi^+\rangle$ ,  $|\Phi\rangle$ , and  $|\Theta\rangle$  with  $m = 2$  passing through the double slit under various slit separations  $a = 0, 200 \mu\text{m}, 400 \mu\text{m}, 600 \mu\text{m}$ , and  $800 \mu\text{m}$  for slit widths of  $b = 80 \mu\text{m}$  and  $b = 150 \mu\text{m}$ . The conventional Young's double-slit structure is inflexible when manipulating the separation of the double slit. In our Sagnac-type double-slit experiment, the separation of the double slits is determined by the distance  $a$  between the slit center and the optical axis. Therefore, the slit separation is flexible to control and is equal to  $2a$ . Clearly, as the slit separation increases, the fringes gradually become dense and both the twist and displacement become not that obvious in the interferogram of a single-mode OAM state.

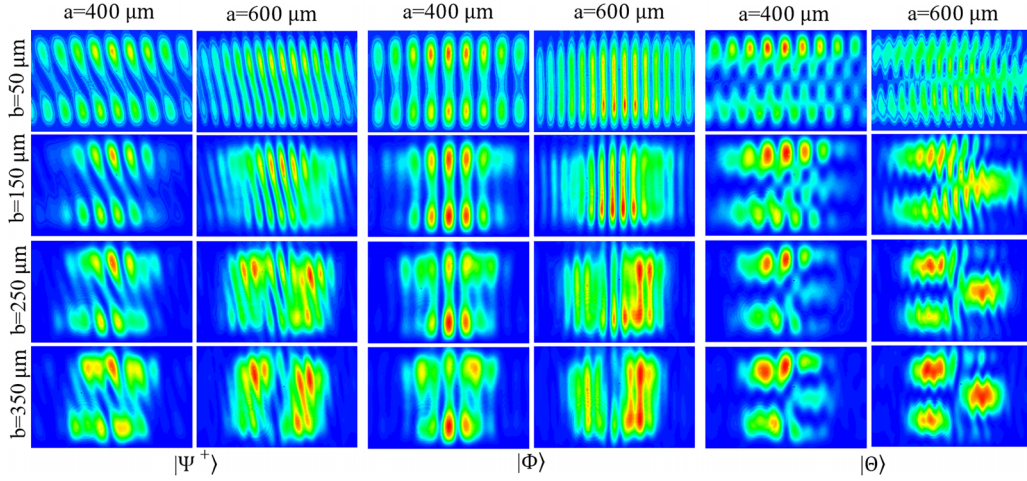


FIG. 5. Experimental results for laser double-slit interference fringes of vortex beams with OAM states  $|\Psi^+\rangle$ ,  $|\Phi\rangle$ , and  $|\Theta\rangle$  under various slit widths  $b = 50 \mu\text{m}$ ,  $150 \mu\text{m}$ ,  $250 \mu\text{m}$ , and  $350 \mu\text{m}$ , when  $a = 400 \mu\text{m}$  and  $600 \mu\text{m}$  and  $m = 2$ .

For the conjugate mode OAM state, as the slit separation increases, both the dark region in the middle of the fringes and the period of fringes diminishes. According to the interferograms of the mixed-mode OAM state, we can know that when the slit separation becomes larger, the dislocations are more easily recognized. We choose the smaller slit separation in Fig. 4 and Fig. 7 because we take into account the effects of the other states at the same time at different topological charges. The results clearly indicate that changing the slit separation is essential for not only making the method more quantitative, but also for distinguishing the multiple OAM states of vortex beams.

Figure 7 shows the experimental results of a single-photon vortex beam passing through a double slit with TC of  $m = 1$ , slit separation  $a = 300 \mu\text{m}$ , and slit width  $b = 150 \mu\text{m}$ . It can be observed that the wave character of each single-photon OAM state is clear and the distribution is similar to the classical distribution. For the single-mode OAM state  $|\Psi^+\rangle$ , twisting interference fringes occur in the right direction and,

for  $|\Psi^-\rangle$ , twisting interference fringes still occur in the left direction, as shown in Figs. 7(a) and 7(b). For conjugate mode  $|\Phi\rangle$ , interference fringes occur as straight stripes with equal spacing, as shown in Fig. 7(c). For the mixed-mode OAM state  $|\Theta\rangle$ , the interference fringes appear to be misplaced in the upper and lower stripes, as described in the laser experiment. All experimental results indicate that the detection of single-photon OAM states is efficient and the double-slit interference based on the Sagnac interferometer method can be utilized to identify the vortex beams.

V. SUMMARY

In conclusion, we proposed a scheme for the double-slit interference with vortex beams based on a Sagnac interferometer by inserting a single slit. We verified the equivalence property between the proposed scheme and the traditional structure of Young’s double-slit interference by measuring the single-mode OAM state of vortex beams. To test the capability

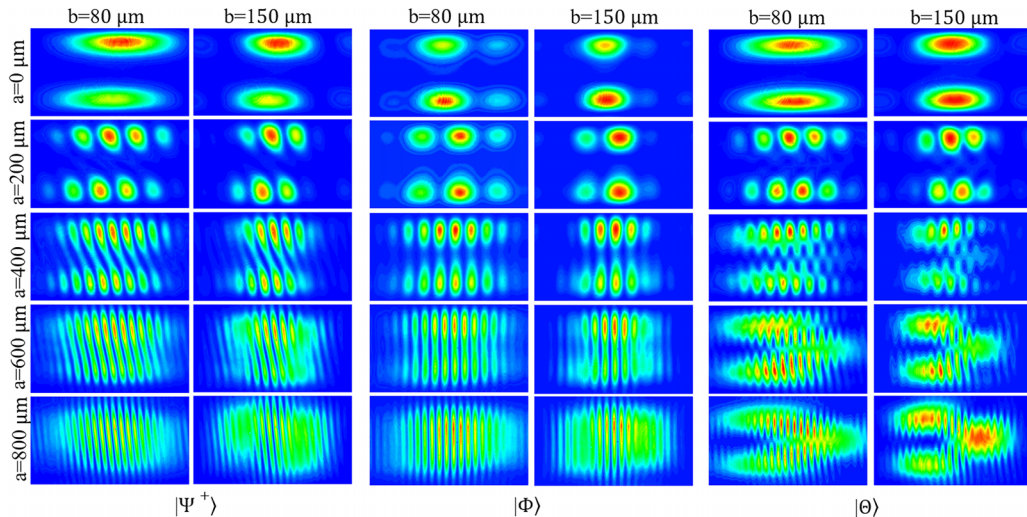


FIG. 6. Experimental results for laser double-slit interference fringes of vortex beams with OAM states  $|\Psi^+\rangle$ ,  $|\Phi\rangle$ , and  $|\Theta\rangle$  under various slit separations  $a = 0 \mu\text{m}$ ,  $200 \mu\text{m}$ ,  $400 \mu\text{m}$ ,  $600 \mu\text{m}$ , and  $800 \mu\text{m}$ , when  $b = 80 \mu\text{m}$  and  $150 \mu\text{m}$  and  $m = 2$ .

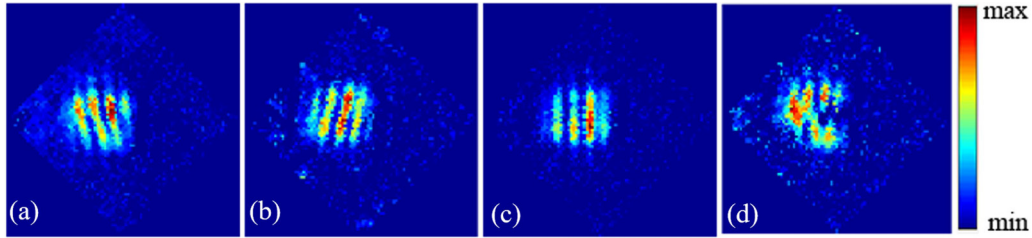


FIG. 7. Experimental results for single-photon double-slit double-slit interference fringes of vortex beams with OAM states (a)  $|\Psi^+\rangle$ , (b)  $|\Psi^-\rangle$ , (c)  $|\Phi\rangle$ , and (d)  $|\Theta\rangle$  for the value of the TC  $m = 1$ .

of our scheme to measure vortex beams, we analyzed vortex beams with different modes' OAM states at the laser and single-photon levels. The results demonstrate that the interference pattern can not only indicate the TC carried by the vortex beams but also identify and distinguish each of the OAM states. In addition, we investigated the effects of slit parameters on the interference pattern of the vortex beams. Our scheme provides an easier experimental platform for studies on single-photon vortex beams in a double-slit experiment.

#### ACKNOWLEDGMENTS

This work is supported by the National Natural Science Foundation of China (Grant No. 92365115).

#### APPENDIX: EFFECTS OF THE RELATIVE PHASE ON DOUBLE-SLIT INTERFERENCE FRINGES OF THE OAM STATES

The conventional Young's double-slit structure has difficulty in varying the phase between double slits. In our double-

slit experiment, we could continuously and accurately vary the phase between the double slits by changing the relative phase between the two arms of the Sagnac interferometer as shown in Fig. 3(c). In Fig. 8, we observe the interference intensities of the different mode OAM states  $|\Psi^+\rangle$ ,  $|\Phi\rangle$ , and  $|\Theta\rangle$  with  $m = 2$  passing through the double slit under various phase differences  $\theta = 0 \sim 2\pi$  in  $\pi/4$  steps for a fixed value of the slit separation  $a = 500 \mu\text{m}$  and slit width  $b = 50 \mu\text{m}$ . The results clearly show that, for the three types of OAM states, the interference fringes are shifted. It shifts a half stripe in  $\theta = \pi$  and thereafter shifts to the next bright stripe after  $\theta = \pi$  as indicated by the black dotted lines in Fig. 8. The results indicate that the double-slit experiment based on the Sagnac interferometer can easily capture the changes in the double-slit interference pattern of the vortex beams caused by a change in the phase difference. However, it is difficult to observe successive fringes shift in conventional double-slit structures. In our device, the regularity of the fringe shifts caused by the change in the phase difference can be clearly displayed.

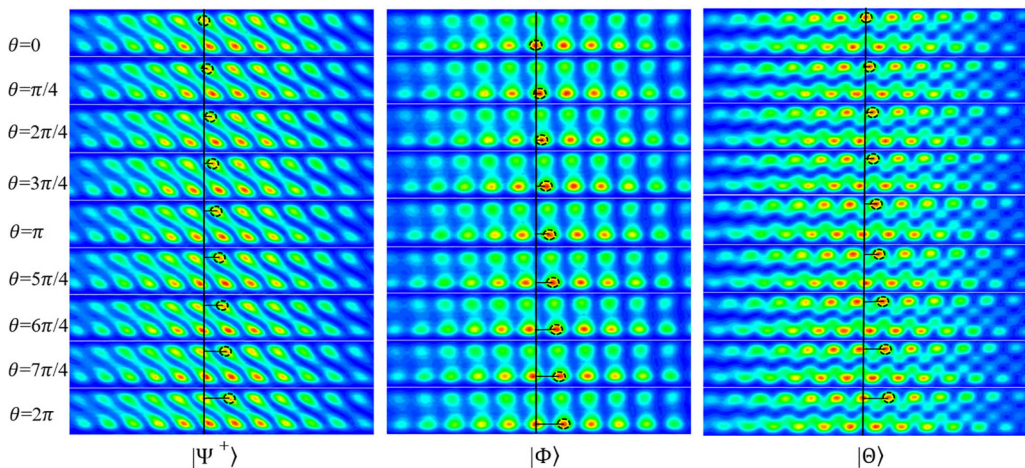


FIG. 8. Experimental results of double-slit interferograms with different mode OAM states  $|\Psi^+\rangle$ ,  $|\Phi\rangle$ , and  $|\Theta\rangle$  under various phases of double slit  $\theta = 0-2\pi$  in  $\pi/4$  steps.

[1] L. Allen, M. W. Beijersbergen, R. J. C. Spreeuw, and J. P. Woerdman, Orbital angular momentum of light and transformation of Laguerre-Gaussian laser modes, *Phys. Rev. A* **45**, 8185 (1992).

[2] J. Wang, J.-Y. Yang, I. M. Fazal, N. Ahmed, Y. Yan, Y. Ren, Y. Yue, S. Dolinar, M. Tur, and A. E. Willner, Terabit free-space data transmission employing orbital angular momentum multiplexing, *Nat. Photonics* **6**, 488 (2012).

- [3] N. Bozinovic, Y. Yue, Y. Ren, M. Tur, P. Kristensen, H. Huang, A. E. Willner, and S. Ramachandran, Terabit-scale orbital angular momentum mode division multiplexing in fibers, *Science* **340**, 1545 (2013).
- [4] S. Barz, E. Kashefi, A. Broadbent, J. F. Fitzsimons, A. Zeilinger, and P. Walther, Demonstration of blind quantum computing, *Science* **335**, 303 (2012).
- [5] D. G. Grier, A revolution in optical manipulation, *Nature (London)* **424**, 810 (2003).
- [6] L. Paterson, M. P. MacDonald, J. Arlt, W. Sibbett, P. E. Bryant, and K. Dholakia, Controlled rotation of optically trapped microscopic particles, *Science* **292**, 912 (2001).
- [7] V. D'Ambrosio, N. Spagnolo, L. Del Re, S. Slussarenko, Y. Li, L. C. Kwek, L. Marrucci, S. P. Walborn, L. Aolita, and F. Sciarrino, Photonic polarization gears for ultra-sensitive angular measurements, *Nat. Commun.* **4**, 2432 (2013).
- [8] M. P. J. Lavery, F. C. Speirits, S. M. Barnett, and M. J. Padgett, Detection of a spinning object using light's orbital angular momentum, *Science* **341**, 537 (2013).
- [9] D. Wei, J. Guo, X. Fang, D. Wei, R. Ni, P. Chen, X. Hu, Y. Zhang, W. Hu, Y. Q. Lu *et al.*, Multiple generations of high-order orbital angular momentum modes through cascaded third-harmonic generation in a 2D nonlinear photonic crystal, *Opt. Express* **25**, 11556 (2017).
- [10] M. Jiang, H. Lin, L. Zhuo, W. Zhu, H. Guan, J. Yu, H. Lu, J. Tan, and Z. Chen, Chirality induced asymmetric spin splitting of light beams reflected from an air-chiral interface, *Opt. Express* **26**, 6593 (2018).
- [11] M. Erhard, M. Malik, and A. Zeilinger, A quantum router for high-dimensional entanglement, *Quantum Sci. Technol.* **2**, 014001 (2017).
- [12] A. Mair, A. Vaziri, G. Weihs, and A. Zeilinger, Entanglement of the orbital angular momentum states of photons, *Nature (London)* **412**, 313 (2001).
- [13] G. Molina-Terriza, J. P. Torres, and L. Torner, Management of the angular momentum of light: Preparation of photons in multidimensional vector states of angular momentum, *Phys. Rev. Lett.* **88**, 013601 (2001).
- [14] B. Nape, A. Ndagano, and A. Forbes, Erasing the orbital angular momentum information of a photon, *Phys. Rev. A* **95**, 053859 (2017).
- [15] W. Zhang, J. Gao, D. Zhang, Y. He, T. Xu, R. Fickler, and L. Chen, Free-space remote sensing of rotation at photon-counting level, *Phys. Rev. Appl.* **10**, 044014 (2018).
- [16] V. Boyer, A. M. Marino, and P. D. Lett, Generation of spatially broadband twin beams for quantum imaging, *Phys. Rev. Lett.* **100**, 143601 (2008).
- [17] M. Mirhosseini, M. Malik, Z. Shi, and R. W. Boyd, Efficient separation of the orbital angular momentum eigenstates of light, *Nat. Commun.* **4**, 2781 (2013).
- [18] M. Gecevičius, R. Drevinskasa, M. Beresna, and P. G. Kazansky, Single beam optical vortex tweezers with tunable orbital angular momentum, *Appl. Phys. Lett.* **104**, 231110 (2014).
- [19] T. Young, XIV. An account of some cases of the production of colours, not hitherto described, *Philos. Trans. R. Soc. London* **92**, 387 (1802).
- [20] M. Bauer, On time and space double-slit experiments, *Am. J. Phys.* **82**, 1087 (2014).
- [21] F. Lindner, M. G. Schatzel, H. Walther, A. Baltuška, E. Goulielmakis, F. Krausz, D. B. Milošević, D. Bauer, W. Becker, and G. G. Paulus, Attosecond double-slit experiment, *Phys. Rev. Lett.* **95**, 040401 (2005).
- [22] F. Gori, M. Santarsiero, R. Borghi, and E. Wolf, Effects of coherence on the degree of polarization in a Young interference pattern, *Opt. Lett.* **31**, 688 (2006).
- [23] Z. Chen and J. Pu, Degree of polarization in Young's double-slit interference experiment formed by stochastic electromagnetic beams, *J. Opt. Soc. Am. A* **24**, 2043 (2007).
- [24] H. I. Sztul and R. R. Alfano, Double-slit interference with Laguerre-Gaussian beams, *Opt. Lett.* **31**, 999 (2006).
- [25] Y. Li, X.-L. Wang, Z. Hu, L.-J. Kong, K. Lou, B. Gu, C. Tu, and H.-T. Wang, Young's two-slit interference of vector light fields, *Opt. Lett.* **37**, 1790 (2012).
- [26] J. L. Qi, W. H. Wang, X. Li, X. Wang, W. Sun, J. Liao, and Y. Nie, Double-slit interference of radially polarized vortex beams, *Opt. Eng.* **53**, 044107 (2014).
- [27] T. Chen, X. Lu, J. Zeng, Z. Wang, H. Zhang, C. Zhao, B. Hoenders, and Y. Cai, Young's double-slit experiment with partially coherent vortex beams, *Opt. Express* **28**, 38106 (2020).
- [28] M. Aili, X.-X. Chen, P. Liu, J.-Z. Yang, X. Guo, J. Li, Z. Meng, Q.-Y. Wu, and A.-N. Zhang, Characterizing interference effects of vortex beams based on the Sagnac interferometer, *Phys. Rev. A* **106**, 023715 (2022).
- [29] L. Allen, M. J. Padgett, and M. Babiker, IV The orbital angular momentum of light, *Prog. Opt.* **39**, 291 (1999).
- [30] M. Lax, W. H. Louisell, and W. B. McKnight, From Maxwell to paraxial wave optics, *Phys. Rev. A* **11**, 1365 (1975).
- [31] F.-X. Wang, J. Wu, W. Chen, Z.-Q. Yin, S. Wang, G.-C. Guo, and Z.-F. Han, Controlled-phase manipulation module for orbital-angular-momentum photon states, *Opt. Lett.* **43**, 349 (2018).
- [32] P. Kumar and N. K. Nishchal, Modified Mach-Zehnder interferometer for determining the high-order topological charge of Laguerre-Gaussian vortex beams, *J. Opt. Soc. Am. A* **36**, 1447 (2019).
- [33] J. W. Goodman, *Introduction to Fourier Optics*, 2nd ed. (McGraw-Hill, New York, 1988).
- [34] X. Guo, Z. Meng, J. Li, J.-Z. Yang, M. Aili, and A.-N. Zhang, The interference properties of single-photon vortex beams in Mach-Zehnder interferometer, *Appl. Phys. Lett.* **119**, 011103 (2021).
- [35] M. F. Duarte, M. A. Davenport, D. Takhar, J. N. Laska, T. Sun, K. F. Kelly, and R. G. Baraniuk, Single-pixel imaging via compressive sampling, *IEEE Signal Process.* **25**, 83 (2008).
- [36] Y. Bromberg, O. Katz, and X. Silberberg, Ghost imaging with a single detector, *Phys. Rev. A* **79**, 053840 (2009).
- [37] Z. B. Zhang, X. Ma, and J. G. Zhong, Single-pixel imaging by means of Fourier spectrum acquisition, *Nat. Commun.* **6**, 6225 (2015).
- [38] G. A. Howland, D. J. Lum, M. R. Ware, and J. C. Howell, Photon counting compressive depth mapping, *Opt. Express* **21**, 23822 (2013).
- [39] P. A. Morris, R. S. Aspden, J. E. C. Bell, R. W. Boyd, and M. J. Padgett, Imaging with a small number of photons, *Nat. Commun.* **6**, 5913 (2015).
- [40] Z. B. Zhang, X. Y. Wang, G. A. Zheng, and J. G. Zhong, Hadamard single-pixel imaging versus Fourier single-pixel imaging, *Opt. Express* **25**, 19619 (2017).